



HAL
open science

From graph theory and geometric probabilities to a representative width for three-dimensional detonation cells

Vianney Monnier, Pierre Vidal, Vincent Rodriguez, Ratiba Zitoun

► **To cite this version:**

Vianney Monnier, Pierre Vidal, Vincent Rodriguez, Ratiba Zitoun. From graph theory and geometric probabilities to a representative width for three-dimensional detonation cells. 2023. hal-04056649v1

HAL Id: hal-04056649

<https://hal.science/hal-04056649v1>

Preprint submitted on 3 Apr 2023 (v1), last revised 31 Jul 2023 (v2)

HAL is a multi-disciplinary open access archive for the deposit and dissemination of scientific research documents, whether they are published or not. The documents may come from teaching and research institutions in France or abroad, or from public or private research centers.

L'archive ouverte pluridisciplinaire **HAL**, est destinée au dépôt et à la diffusion de documents scientifiques de niveau recherche, publiés ou non, émanant des établissements d'enseignement et de recherche français ou étrangers, des laboratoires publics ou privés.

From graph theory and geometric probabilities to a representative width for three-dimensional detonation cells

Vianney Monnier*, Pierre Vidal, Vincent Rodriguez, Ratiba Zitoun

*Institut Pprime, UPR 3346 CNRS, Fluid, Thermal and Combustion Sciences Department,
ENSMA, Téléport 2, 1 Av. Clément Ader, Chasseneuil-du-Poitou, 86360, France*

Abstract

We present a model for predicting a representative width for the three-dimensional cells observed on detonation fronts in reactive gases. Its physical premise is that the dynamics of the transverse waves of irregular cells obeys a stochastic process both stationary and ergodic and produces the same burnt mass per unit of time as the average planar steady ZND process. Graph theory then defines an ideal cell whose grouping is equivalent to the actual 3D cellular front, geometric probabilities determine the mean burned fraction that parameterizes the model, and ZND calculations close the problem with the time-position relationship of a fluid element in the ZND reaction zone. The model is limited to detonation reaction zones whose sole ignition mechanism is adiabatic shock compression, such as those of the mixtures with H_2 , C_3H_8 or C_2H_4 as fuels considered in this work. Indeed, the comparison of their measured and calculated widths shows an agreement better than or within the accepted experimental uncertainties, depending on the quality of the chemical kinetic scheme used for the ZND calculations. However, the comparison for $CH_4:O_2$ mixtures shows high overestimates, indirectly confirming that the detonation reaction zones in these mixtures certainly include other ignition mechanisms contributing to the combustion process, such as turbulent diffusion. In these situations, the cell mean width derived from longitudinal soot recordings shows a very large scatter and may thus not be a relevant detonation characteristic length. The model is easily implementable as a post-process of ZND profiles and provides fast estimates of the cell width, length and reaction time.

*Corresponding author: vianney.monnier@ensma.fr

1. Introduction

First identified experimentally in the late 1950s [1], the cellular structure of the detonation reaction zone in gases is viewed today as an example of nonlinear instability of combustion waves in compressible reactive fluids, *e.g.* [2]. It is now recognized that its physical representation can only be three-dimensional. Experiments on constant-velocity detonations in straight tubes are the usual method to characterize the basic phenomenology of this structuring, namely a grouping of Mach waves consisting of forward propagating convex shocks bounded by transversely propagating shocks, respective to the tube axis. Experimental and numerical analyses, *e.g.* [3, 4], evidence that the front views of these detonation cells usually form irregular polygonal patterns, in particular, if their number on the front surface is sufficiently large. That is observed typically in tubes with cross sections large enough because the usual cell descriptor, namely a mean width $\bar{\lambda}_C$, decreases as the initial pressure p_0 of the gas increases. The modelling framework then often includes hydrodynamics and chemical kinetics solely and neglects viscosity, for example from boundary layers and turbulence. A topic of debate is whether a single characteristic length is sufficient to characterize these 3D irregular cells. In the following, we assume that such is $\bar{\lambda}_C$, and we propose a model for predicting it based on the analysis outlined from our experimental recordings of detonation cells [3, 5].

Classically, investigations rest on recordings on soot-coated foils placed longitudinally against the inner wall(s) of the tube. The erosion of the coating by the moving intersections of the transverse and longitudinal shocks with the foil draws lozenges whose statistical analysis defines the mean width $\bar{\lambda}_C$. Mixtures of light fuels and oxygen highly diluted with a monoatomic inert gas, such as argon, give regular lozenges, and heavy fuels diluted with nitrogen irregular ones [6–9]. The χ parameter measures this longitudinal irregularity, *i.e.*, the higher χ , the more irregular the lozenges [2, 10, 11]. Front-view recordings can be easily obtained from the impact of the detonation on a soot-coated foil placed perpendicular to the tube axis [1]. They show polygonal patterns whose edges represent the positions of the transverse waves at the instant of impact. The observations indicate that these geometric properties depend markedly on the initial pressure p_0 , temperature T_0 and composition of the mixture [12–14], and the cross-section shape of the tube. Thus, the regularity of the lozenges should be considered a relative notion because of this dependence and the possible contradictory information from longitudinal and front-view recordings.

For example [3], for the mixture $2\text{H}_2 + \text{O}_2 + 2\text{Ar}$, the front-view recordings show irregular polygons at large-enough p_0 regardless of the cross-section shape, but alternate square and rectangular regular patterns at small-enough p_0 in a square cross section. The longitudinal recordings show regular cells regardless of p_0 and the cross-section shape. As p_0 decreases, the regular arrangement on the longitudinal recordings remains qualitatively the same in the round cross section, whereas lines emerge between the cell rows in the square cross section, representing the impacts of transverse waves propagating perpendicular to the recording wall, coherently with the information from the front views.

The cell widths $\bar{\lambda}_C$ decrease with increasing p_0 and become independent of the cross-

section shape if the number of cells per surface area is large enough, that is, when p_0 is greater than a limit that may depend on the cross-section area. Below this limit, the values of $\bar{\lambda}_C$ are smaller in the square cross section at the same p_0 , with a difference that increases with decreasing p_0 . The cross-section shape has no apparent effect on the cell aspect ratio above the limiting p_0 , but the cells are slimmer in the square cross section below it. Thus, the cell dynamics at the walls of a tube at large-enough p_0 or cell number may not represent that on the entire detonation front, and information from longitudinal recordings may not be sufficient alone to describe the geometric properties of the cellular structure.

Marginal detonation regimes are observed for tube transverse dimensions or p_0 sufficiently small so that the number of cells on the front is not too large. Therefore, regular patterns on front-view recordings are exclusive of marginal detonations in mixtures with light fuels contained in tubes with square or rectangular cross sections. Irregular patterns on front-view recordings do not necessarily indicate multi-cellular regimes, *e.g.*, Chapman-Jouguet (CJ), since this irregularity depends on the cross-section shape at sufficiently small p_0 and is inherent to numbers of cells sufficiently large.

Nevertheless, the mean width $\bar{\lambda}_C$ is still considered to be a useful characteristic length for the analysis of detonation dynamics, and we propose a heuristic model for predicting it for constant-velocity detonations in constant cross-section tubes if the number of cells or p_0 is sufficiently large. Its three ingredients are graph theory, geometric probabilities and the Zel'dovich-Von Neuman-Döring (ZND) model of planar detonation. Its principle assumes a global equivalence of the ZND and cellular combustion processes, relative to their respective reaction times, expressed by basic conservation and action laws, with the limitation that both processes should be adiabatic. As is discussed in Section 5, this limits the predictive capacity of the model to detonation cells whose longitudinal soot recordings show longitudinally regular to irregular lozenges, *i.e.* excludes the cases of highly irregular lozenges.

The model is not intended to explain how detonation reaction zones become unstable. This still poses difficulties for theoretical approaches based on perturbation techniques (Sect. 5), *e.g.*, [15], while numerical simulations still require large computational resources. We have considered a global approach that could readily provide a mean width sufficiently accurate for practical purposes without detailing the complex wave interactions of the cellular structure.

In Section 2, we express the physical premise that the unsteady 3D process for irregular cells is stochastic and should produce on average the same burnt mass as the steady planar ZND process per unit of time. In Section 3, we implement graph theory to define an ideal cell whose grouping is equivalent to the real 3D cellular front [3], geometric probabilities to determine the mean burnt fraction that parameterizes the model, and the ZND model with detailed schemes of chemical kinetics to compute the relation time-position of a fluid element in the ZND steady reaction zone, which closes the problem of determining $\bar{\lambda}_C$. In Section 4 we compare measured and calculated $\bar{\lambda}_C$ depending on the reactive mixture and the chemical kinetics scheme. In Section 5, we discuss the model, and we conclude. We describe the ZND model equations and their numerical integration in the Appendix A, and we collect the notation in the Appendix B.

2. Model

The basic assumption is that the cellular and ZND processes burn the fresh mixture at the same mass rate for sufficiently long periods and with the same projected area of the detonation front. The ZND model of this work is that for constant-velocity detonation, *i.e.* a steady planar reaction zone induced by a planar shock of constant velocity D . This ZND process is a valid average of the cellular process if the number of cells is very large. We choose as the origin of distances x in the reference frame of the laboratory an arbitrary initial position $L_0 = 0$ of the ZND front and as the origin of times t the instant $t_0 = 0$ when the fluid elements enter the ZND reaction zone. Thus, at an instant $t > 0$, the position of the front is $L(t) = Dt$ and the distance measured from the front is $z = Dt - x$. Steadiness is the invariance of any variable f with respect to $L(t)$ at a constant relative distance z in the reaction zone, so f is function of a single independent variable, namely t or z . The relative position $z_m(t)$ of a fluid element, or the period $t_m(z)$ elapsed from the front to this position, are calculated by integrating the material speed with the ZND equations (App. A).

We refer to below as a complete reaction time the period necessary to completely burn all fluid elements captured by a front at $t_0 = 0$ and through the same reference surface area. Let Δt_C the period during which the ZND front travels the distance \bar{L}_C representing the length of the mean cell. For the self-sustained detonation propagating at the Chapman-Jouguet (CJ) velocity D_{CJ} ,

$$\bar{L}_C = D_{CJ} \Delta t_C. \quad (1)$$

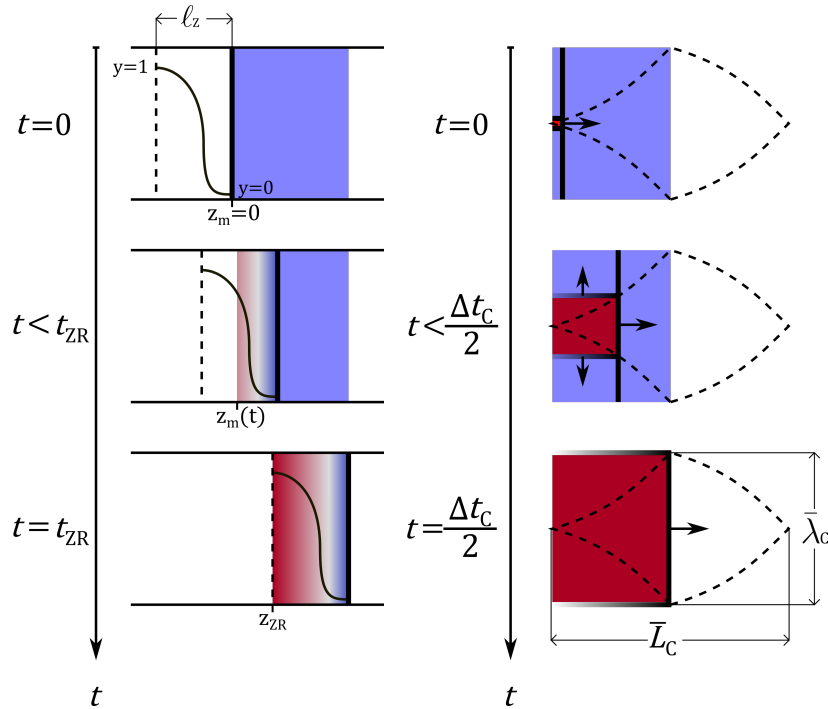


Figure 1: Left: ZND process. Right: cellular model process

In the ZND process, denoting by t_{ZR} its complete reaction time, the fluid elements entered in the reaction zone during the period $0 < t \leq t_{\text{ZR}}$ can only be partially burnt at t_{ZR} (Fig. 1-left). That results in the mean ZND burnt fraction \bar{y}_{Z} and reaction rate $\bar{y}_{\text{Z}}/t_{\text{ZR}}$. In the cellular process, the front is a grouping of forward-convex waves whose forefront velocities for irregular cells randomly vary about the ZND mean velocity, such as D_{CJ} , *e.g.* [16]. Their boundaries are the intersections with transverse waves that sweep the surfaces of the slower forward waves. For mixtures whose longitudinal soot recordings show lozenges with not too high irregularity, such as those with the light fuel H_2 or the heavier hydrocarbon fuels C_2H_4 or C_3H_8 , the high-speed recordings indicate that the local combustion rate is much more rapid in the regions behind the transverse waves and the faster forward waves, that is, much faster than the mean cellular rate for mixtures, *e.g.*, [17–20]. The dominant ignition mechanism is then the adiabatic shock compression, and a limiting symmetry argument then suggests that the complete reaction time, as defined above, of the ideal cell should be half the cell time $\Delta t_{\text{C}}/2$. Indeed, the period $[0, \Delta t_{\text{C}}/2]$ is that necessary, on average, for the transverse waves to sweep a projected front area equivalent to the maximum area of the ideal cell, which, by symmetry, occurs every cell half length $\bar{L}_{\text{C}}/2$. Thus, during this period, they cover the surface of the ideal cell, and they can capture and burn all the fluid elements that have crossed the lower-velocity front surfaces since t_0 (Fig. 1-right). That results in the mean cell burnt fraction \bar{y}_{C} and reaction rate $2/\Delta t_{\text{C}}$ – and not $\bar{y}_{\text{C}} \times 2/\Delta t_{\text{C}}$. The means of the mass fractions y_{Z} and y_{C} are relative to periods elapsed since $t_0 = 0$. They write

$$\bar{y}_{\text{Z}} = \frac{1}{t_{\text{ZR}}} \int_0^{t_{\text{ZR}}} y_{\text{Z}}(t) dt, \quad \bar{y}_{\text{C}} = \frac{2}{\Delta t_{\text{C}}} \int_0^{\Delta t_{\text{C}}/2} y_{\text{C}}(t) dt, \quad (2)$$

where the subscripts Z and C denote the ZND and the cellular processes. The first time average above also applies to any variable, for example, the material speed $U_{\text{Z}}(t) = dz_{\text{m}}(t)/dt$ at the instant t or the position $z_{\text{m}}(t)$ of a fluid element in the ZND reaction zone. This defines the ZND complete reaction length ℓ_{ZR} by

$$\ell_{\text{ZR}} = \int_0^{t_{\text{ZR}}} U_{\text{Z}}(t) dt = \bar{U}_{\text{Z}} t_{\text{ZR}}, \quad \bar{U}_{\text{Z}} = \frac{\ell_{\text{ZR}}}{t_{\text{ZR}}}, \quad (3)$$

where \bar{U}_{Z} denotes the mean of $U_{\text{Z}}(t)$. With v denoting the specific volume, and v_0 its initial value, the relation of mass conservation (App. A)

$$v_{\text{Z}} D_{\text{CJ}} = v_0 U_{\text{Z}} \quad (4)$$

considered at any position $z_{\text{m}}(t)$ can also be averaged, and (3) rewrites

$$\ell_{\text{ZR}} = \frac{\bar{v}_{\text{Z}}}{v_0} D_{\text{CJ}} \times t_{\text{ZR}}, \quad (5)$$

$$\bar{v}_{\text{Z}}(\bar{y}_{\text{Z}}) = (1 - \bar{y}_{\text{Z}}) v_{\text{H}} + \bar{y}_{\text{Z}} v_{\text{CJ}}. \quad (6)$$

The relation (6) results from (4) and the averaging of the volume additivity relation $v = \sum y_i v_i$, where v_i and y_i denote the specific volume and the mass fraction of the chemical

species i , and v_H and v_{CJ} denote the specific volumes at the ZND shock (subscript H) and the reaction end positions (subscript CJ for a self-sustained reaction zone, *i.e.* this work). The ZND reaction zone thus reduces to an induction layer without chemical reactions and a main reaction layer that concentrates the burnt mass. Per unit of surface area, these masses are $M_H = (U_H/v_H)t_{ZI}$ and $M_B = (U_{CJ}/v_{CJ})\delta t_{ZR}$ respectively, where t_{ZI} and δt_{ZR} are the crossing times of these layers ($t_{ZR} = t_{ZI} + \delta t_{ZR}$). The mean fraction \bar{y}_Z is the ratio M_B/M_Z , where $M_Z = M_H + M_B = (\bar{U}_Z/\bar{v}_Z)t_{ZR}$ is the total mass in the ZND reaction zone, and it is also the ratio $\delta t_{ZR}/t_{ZR}$ since U/v is constant (4).

The equality of the cellular and ZND average reaction rates implies that of their average reaction progress variables \bar{y}_C and \bar{y}_Z with respect to their reaction times $\Delta t_C/2$ and t_{ZR} , so

$$\frac{2}{\Delta t_C} = \frac{\bar{y}}{t_{ZR}}, \quad (7)$$

where \bar{y} denotes $\bar{y}_C = \bar{y}_Z$. The combination of (1) with (7) gives the relation (8) between the cell mean length \bar{L}_C and the ZND complete reaction time t_{ZR} , which, with (5) and (6), gives the relation (9) between \bar{L}_C and the ZND complete reaction length ℓ_{ZR} ,

$$\bar{L}_C(\bar{y}, t_{ZR}) = k_1 \times t_{ZR}, \quad k_1(\bar{y}) = \frac{2}{\bar{y}} D_{CJ}, \quad (8)$$

$$\bar{L}_C(\bar{y}, \ell_{ZR}) = k_2 \times \ell_{ZR}, \quad k_2(\bar{y}) = \frac{2}{\bar{y}} \frac{v_0}{\bar{v}_Z(\bar{y})}. \quad (9)$$

In the next section, graph theory is used to define a cellular pattern statistically equivalent to those on an irregular 3D cellular front, hence the ideal cell to which geometric probabilities are applied to obtain \bar{y} (Fig. 2). The cell length \bar{L}_C is then determined by the intersection of the curves $L_1(z)$ and $L_2(z)$,

$$L_1(z) = k_1 \times t_m(z), \quad (10)$$

$$L_2(z) = k_2 \times z, \quad (11)$$

which represent the functional dependencies of the front position $L(t) = D_{CJ}t$ (1) on the distance $z_m(t)$ of a fluid element in the ZND reaction zone. The function $t_m(z)$ in (10) is the relation time-position of a fluid element in the ZND reaction zone, which is determined by classical ZND numerical calculations with a detailed chemical kinetic scheme (App. A). The intersections thus also determine t_{ZR} and ℓ_{ZR} . The cell mean width $\bar{\lambda}_C$ is obtained from additional geometry considerations (Sect. 3) that define the width-to-length aspect ratio $a = \bar{\lambda}_C/\bar{L}_C$. Figure 6 shows this principle as the intersection of the transverse-wave mean distances $\lambda_1(z) = aL_1(z)$ and $\lambda_2(z) = aL_2(z)$.

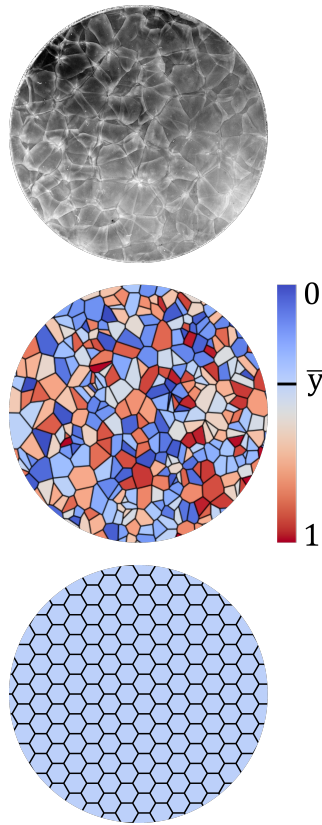


Figure 2: Front views of the cellular structure. Top: soot recording for the $2\text{H}_2 + \text{O}_2 + 2\text{Ar}$ mixture at $p_0 = 30\text{ kPa}$ in a 16 cm^2 round tube. Middle: schematic with randomly distributed face colors representing randomly distributed burnt mass fraction $y(t)$. Bottom: equivalent hexagon-patterned tessellation with burnt mean mass fraction $\bar{y} = 0.38498$ (Sect. 3).

3. Graph theory and geometric probabilities

In our preliminary analysis [3], we considered the distribution of a same pattern on the detonation front surface, for example, rectangle, pentagon, hexagon, *etc.*, to be independent of the front position if the cell number F , that is the initial pressure p_0 , is sufficiently large. Indeed, several experiments carried out in the same conditions should return the same distribution. We used elements from planar graph theory to show that these front views are equivalent to tessellations of hexagons. This was obtained by combining the physical condition that only three transverse waves can intersect with the mathematical limit at large F of the Descartes-Euler-Poincaré relation $F - E + V = 2$ that connects the numbers of faces F (the cells), edges E (the transverse waves) and vertices V (the edge intersections) in a tessellation. For three-edge vertices, $2E = 3V$, so the limit at large F of the edge number per face $2E/F$ is 6 (Fig. 2). One consequence is that a cell counting on an experimental recording gives the estimate of the cell mean width

$$\bar{\lambda}_C = \frac{3 \ln 3 \sqrt{3}}{\pi} \frac{d_x}{2}, \quad d_x = \sqrt{\frac{8}{3\sqrt{3}} A_C}, \quad A_C = \frac{A_T}{F}, \quad (12)$$

where d_x and A_C are the outer diameter and the area of the hexagon, and A_T the cross-section area of the tube. Another consequence, detailed below, is that a combination of properties of this tessellation of hexagons and geometric probabilities predicts the mean reaction progress variable \bar{y} and hence the cell mean width $\bar{\lambda}_C$ (Sect.2). The premise is that the dynamics of the transverse waves for irregular cells obeys a stochastic process both stationary and ergodic. We substantiate the hexagon limit and the process dynamics in Section 5.

First, we define a control volume with the surface area A_C and the half length $\bar{L}_C/2$ of the ideal cell (1). We denote by M_C the mass contained in this volume, $M(t)$ the mass that has crossed this surface during the period $0 \leq t \leq \Delta t_C/2$, *i.e.* when the front has travelled the distance $L(t) = Dt \leq \bar{L}_C/2$, and, respectively, $A_B(t)$ and $M_B(t)$ the area swept and the mass burnt by the transverse waves during this period (Fig. 1-right). They write

$$M_C = \rho_0 A_C \frac{\bar{L}_C}{2}, \quad M(t) = \rho_0 A_C L(t), \quad M_B(t) = \rho_0 A_B(t) L(t), \quad (13)$$

where ρ_0 denotes the initial specific mass. Thus, the burnt mass fraction y_C is

$$y_C(t) = \frac{M_B(t)}{M(t)} = \frac{A_B(t)}{A_C}, \quad (14)$$

so its mean \bar{y}_C (2) is the mean combustion area respective to the cell area A_C .

Next, we express the stationary ergodicity of the transverse waves viewed as a large set of line segments of different lengths. We assume the successive orientations and lengths of the transverse waves over the propagation period $\Delta t_C/2$ in the same experiment to be statistically identical to those from one experiment to another at the same front position. That ensures that the combustion efficiency is, on average, independent of the experiment

and the front position, which is tantamount to admitting that the transverse waves behave like line segments randomly dropped on the front surface. Thus, \bar{y}_C is the probability that the segments are entirely contained in the cell surface, *i.e.* the non-intersection probability. Its calculation is a classical problem of geometric probabilities, namely Buffon's needle problem extended to a surface with a polyhedral tiling and needle lengths varying between 0 and the largest width of the polyhedron, here for example, the outer diameter d_x of the hexagon.

Many accounts of such problems express a non-intersection probability as a ratio μ_C/μ of measures. The measure μ is the hyper-volume of the space of all possible random values of the independent variables, and μ_C is that of the subspace of those values that ensure the non-intersection of the segments with the edges of the polyhedron. The independent variables are the orientation angle, the maximum length and the center coordinates of the segment, given the polyhedron. The non-intersection constraint confines the segment center to a smaller polyhedron whose shape and area depend on the segment orientation and length. For the hexagon, we extend below to a variable-length segment the solution of Vassallo [21] for a constant-length segment. Because of the clarity of his presentation, we do not reproduce his calculations for brevity. In our notation, the hexagon has an area $A_C = (3\sqrt{3}/2) \times (d_x/2)^2$, the segment angle varies in $[0, 2\pi]$ and its length s in $[0, d_x]$, so the measure is $A_C \times 2\pi \times d_x = 6\pi\sqrt{3}(d_x/2)^3$. Nondimensionalizing the lengths s by the side length $d_x/2$ of the hexagon, and denoting by $r = 2s/d_x$ the non-dimensional segment lengths, we obtain

$$\mu = 6\pi\sqrt{3}, \quad \mu_C = \mu_1 + \mu_2 + \mu_3, \quad \mu_i = \int_{r_{i1}}^{r_{i2}} m_i(r) dr, \quad (15)$$

$$r \in [r_{11} = 0, r_{12} = 1], \quad m_1(r) = 3\pi\sqrt{3} - 12r + r^2 \left(3 - \pi/\sqrt{3}\right), \quad (16)$$

$$r \in [r_{21} = 1, r_{22} = \sqrt{3}], \quad m_2(r) = \pi\sqrt{3}(r^2 + 5) - 9\sqrt{4r^2 - 3} \dots \\ \dots - 2\sqrt{3}(3 + 2r^2) \arcsin(\sqrt{3}/2r), \quad (17)$$

$$r \in [r_{31} = \sqrt{3}, r_{32} = 2], \quad m_3(r) = 2\sqrt{3}(r^2 + 12) \arcsin(\sqrt{3}/r) \dots \\ \dots + 30\sqrt{r^2 - 3} - (8\pi\sqrt{3} + 18) - r^2 \left(3 + 2\pi/\sqrt{3}\right), \quad (18)$$

$$\mu_1 = 10.720, \quad \mu_2 = 1.8374, \quad \mu_3 = 1.1547 \times 10^{-2}, \quad (19)$$

where the m_i s are Vassallo's non-intersection measures for constant segment lengths [21] and the μ_i s ours for segment lengths varying in the intervals $[0, d_x/2]$, $[d_x/2, \sqrt{3}d_x/2]$ and $[\sqrt{3}d_x/2, d_x]$. This gives the non-intersection probability, that is, the mean burnt fraction \bar{y}_C ($\equiv \bar{y}$, Sect.2), by

$$\mu = 32.648, \quad \mu_C = 12.569, \quad \bar{y} = \frac{\mu_C}{\mu} \approx 0.38498. \quad (20)$$

Finally, we obtain the aspect ratio $\bar{\lambda}_C/\bar{L}_C$ by combining stochasticity and, inspired by [22], geometry. Since the transverse waves have a stochastic motion, their positions can be considered to be the same every period Δt_C , so the longitudinal overdriven front waves of the model cellular front should superimpose on each other every distance \bar{L}_C . Equivalently,

these waves can be viewed as the upper surface elements of spheres arranged in the hexagonal closest packing, that is, with alternate layers in the ABAB ... sequence. The sphere diameter is also the distance between the centers of adjacent spheres and the inner diameter d_i of a hexagon, so the ratio \bar{L}_C/d_i comes out as twice the height of the tetrahedral pyramid whose base is the triangle with vertices the centers of the three closest spheres in the same layer. Simple geometry then gives $\bar{L}_C/d_i = \sqrt{8/3}$ and $d_i/d_x = \sqrt{3}/2$. With the first relation (12), that yields the mean cell aspect ratio

$$a = \frac{\bar{\lambda}_C}{\bar{L}_C} = \frac{3 \ln 3}{\pi} \sqrt{\frac{3}{8}} \approx 0.64244, \quad (21)$$

which gives the opening angle 65.4° well representing the measurements on the longitudinal recordings. The intersection of $L_1(z)$ (10) and $L_2(z)$ (11) defines the value of \bar{L}_C in (21).

4. Results

Figures 3 and 4 compare calculated and experimental cell mean widths $\bar{\lambda}_C$.

We have used the experimental values given in the Detonation Database [23]. The red crosses (+) indicate measurements in tubes whose transverse dimension is at least ten times the experimental $\bar{\lambda}_C$, *i.e.* for detonation fronts with at least $\mathcal{O}(100)$ cells, and the gray crosses (\times) otherwise. The first case is closer to the validity condition of our model that the transverse dimension must be large enough compared to $\bar{\lambda}_C$ (*e.g.*, fig.7 in [3]). We found the information on the tube dimension and the measurement uncertainty on the widths (shown as error bars) in the references of the Detonation Database.

The model is valid for a sufficiently large number of cells on the front surface (Sect. 3). The choice in section 4 to retain only the experimental results in tubes whose transverse dimension is at least ten times the experimental $\bar{\lambda}_C$, *i.e.* there should be at least $\mathcal{O}(100)$ cells on the front, is arbitrary and follows from our experimental observations for the sole mixture $2\text{H}_2 + \text{O}_2 + 2\text{Ar}$ [3, 5]. Therefore, further experiments are needed to determine more precisely the constraints on the initial conditions of a given mixture and the tube cross-section area above which the mean width and the front-view cell patterns are independent of the tube.

We carried out the ZND calculations using the Konnov’s [24], San-Diego [25], and FFCM-1 [26] chemical kinetic schemes. We chose H_2 , C_3H_8 , C_2H_4 , or CH_4 as fuels and O_2 as the oxidant, pure or diluted with the diatomic diluent N_2 in its proportion in air ($\text{O}_2 + 3.71\text{N}_2 + 0.048\text{Ar}$), because of their practical importance and the attention they have received from kineticists. We input the same initial pressures and temperatures as in the Detonation Database [23], and table 1 shows which scheme fits which fuel. The object here is not to detail the intrinsic properties of these schemes nor to discuss the differences between their predictions.

Table 1: Compatibility table of the fuels and the chemical kinetic schemes

Fuel	symbol	H_2	C_3H_8	C_2H_4	CH_4
Konnov [24]	◆	yes	yes	yes	yes
San-Diego [25]	●	yes	yes	yes	yes
FFCM-1 [26]	▲	yes	no	no	yes

Two independent elements determine the relevance of the calculated $\bar{\lambda}_C$, namely the model assumptions and the kinetic scheme. Their respective contributions to the differences with the experimental values are difficult to distinguish due to the sensitivity of the detonation characteristic lengths to the chemical kinetics. Our approach to best separate them is to consider as a reference case the mixture $2\text{H}_2 + \text{O}_2$, whose cell widths are both frequently measured and small enough compared to the transverse dimension of most detonation tubes, and whose kinetic schemes have been frequently studied.

The good agreement shown in figure 3-a for the reference case and in figures 3-c to -f for H_2 :Air mixtures for each scheme tends to indicate that the model assumptions are correct, at

least for this fuel mixed with O_2 or air. Figure 5 shows the sensitivities of the temperature profile and $\bar{\lambda}_C$ to the scheme for $2H_2 + O_2$ at 20 kPa. However, the large amount 40% mol. of the monatomic diluent Ar in $2H_2 + O_2$ leads to overestimates of $\bar{\lambda}_C$. A possible interpretation is that, for large dilutions with Ar, the considered schemes are calibrated only for lean mixtures, *e.g.* [27]. Nevertheless, the calculated values have the right magnitude and decreasing trend with increasing p_0 .

The figures 4-a to -d for the hydrocarbon fuels C_3H_8 and C_2H_4 show as good an agreement as for $2H_2 + O_2$ and $2H_2 + Air$. However, the calculations for CH_4 overestimate the measurements, although the schemes are valid for the equivalence ratio considered. Our interpretation involves the very large values of the χ parameter for the $CH_4 + O_2$ mixture, a situation for which a cell mean width, measured or calculated, may not be a relevant characteristic length [2, 10, 11, 28] (Sect. 5).

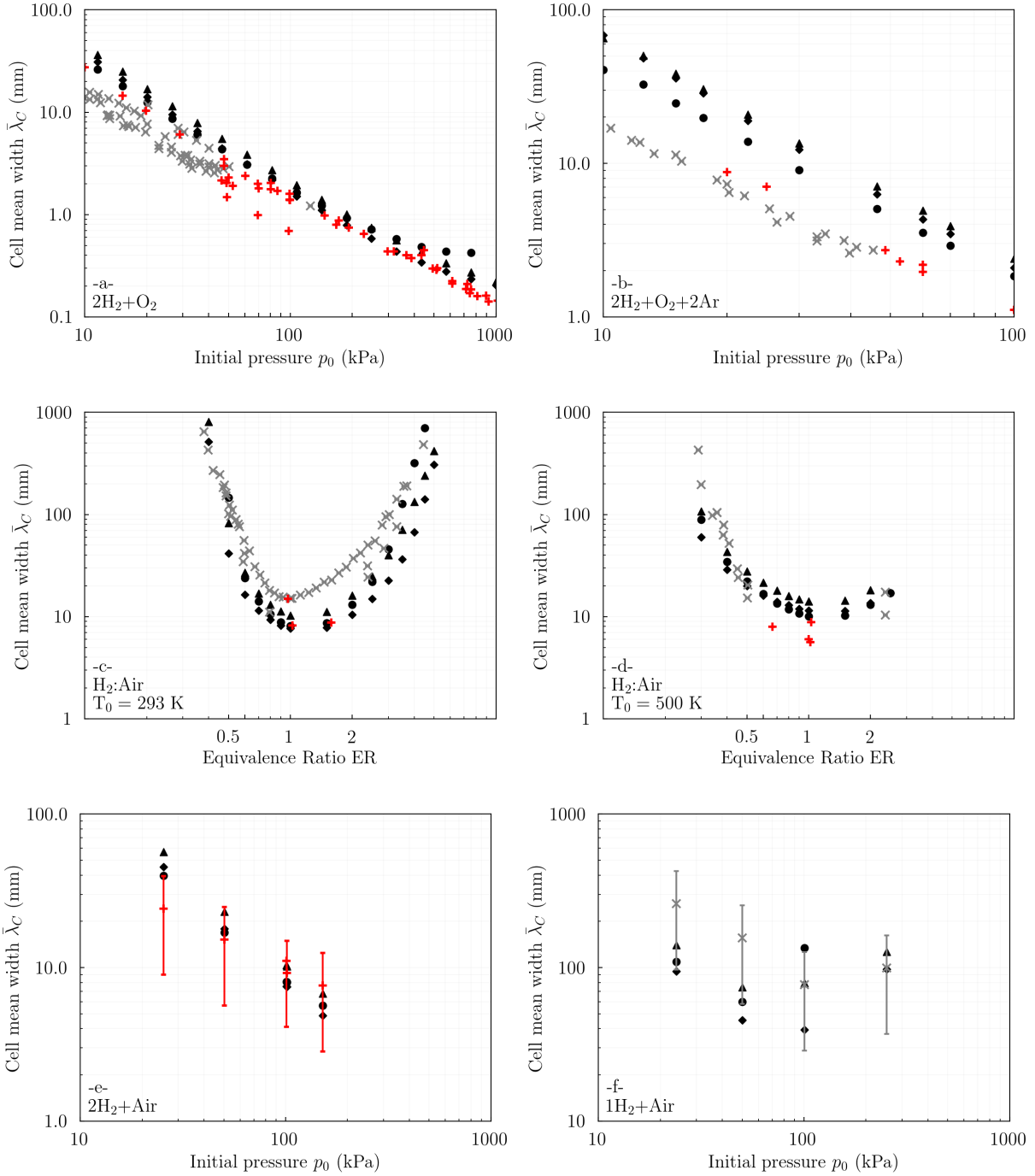


Figure 3: Comparison of calculated and measured cell mean widths $\bar{\lambda}_C$ for H_2 as the fuel. Full and open symbols: calculations using Konnov's [24] (\blacklozenge), the San Diego [25] (\bullet) and the FFCM-1 [26] (\blacktriangle) schemes of chemical kinetics. Crosses: measurements [23] with small ($\leq \mathcal{O}(10)$, red $+$) and large ($\geq \mathcal{O}(10)$, gray \times) ratios $\bar{\lambda}_C/d$, with d_{transv} the transverse dimension of the tubes.

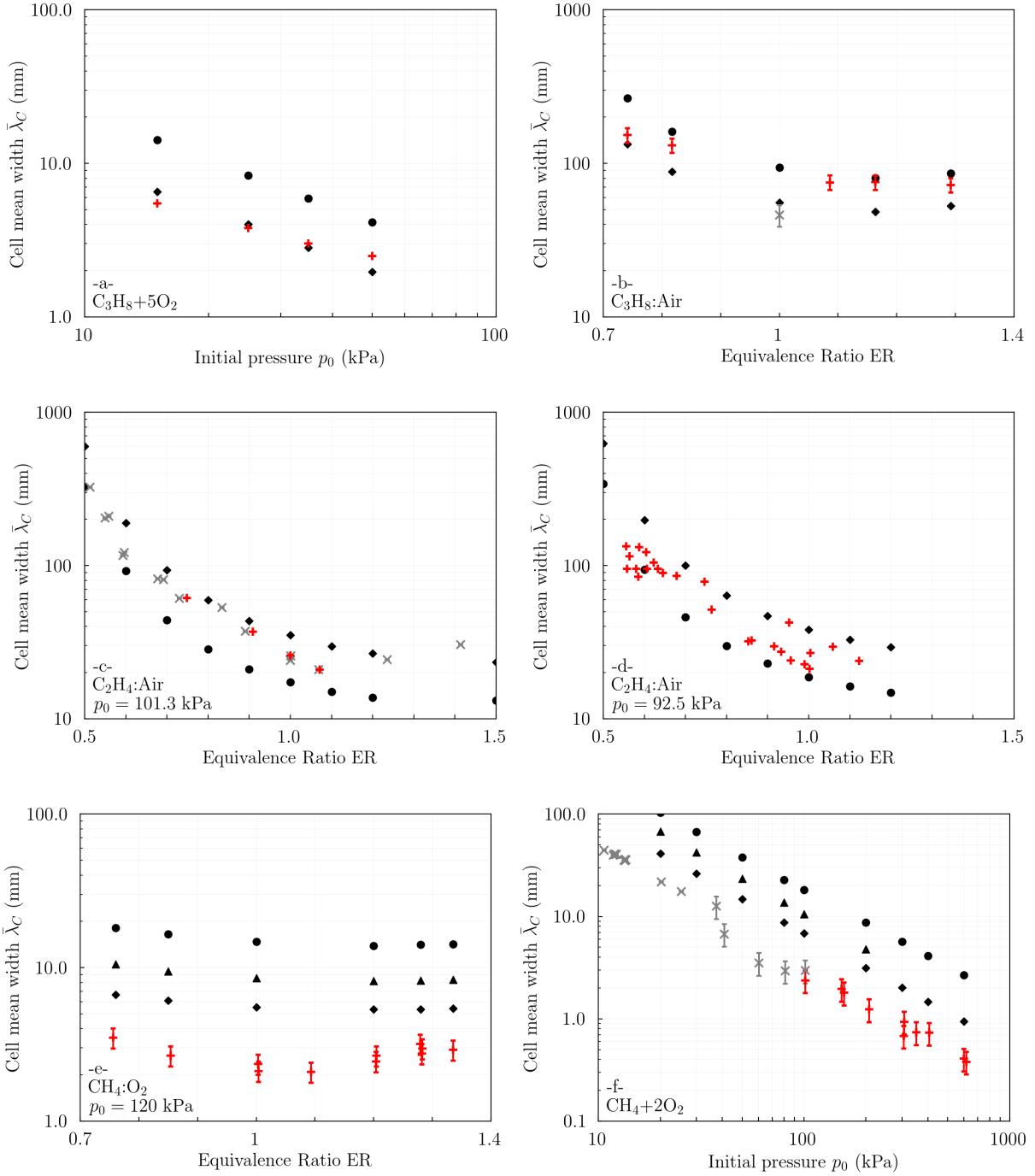


Figure 4: Comparison of calculated and measured cell mean widths $\bar{\lambda}_C$ for hydrocarbon fuels. Full and open symbols: calculations using Konnov's [24] (◆), the San Diego [25] (●) and the FFCM-1 [26] (▲) schemes of chemical kinetics. Crosses: measurements [23] with small ($\leq \mathcal{O}(10)$, red +) and large ($\geq \mathcal{O}(10)$, gray ×) ratios $\bar{\lambda}_C/d_{transv}$, with d_{transv} the transverse dimension of the tubes.

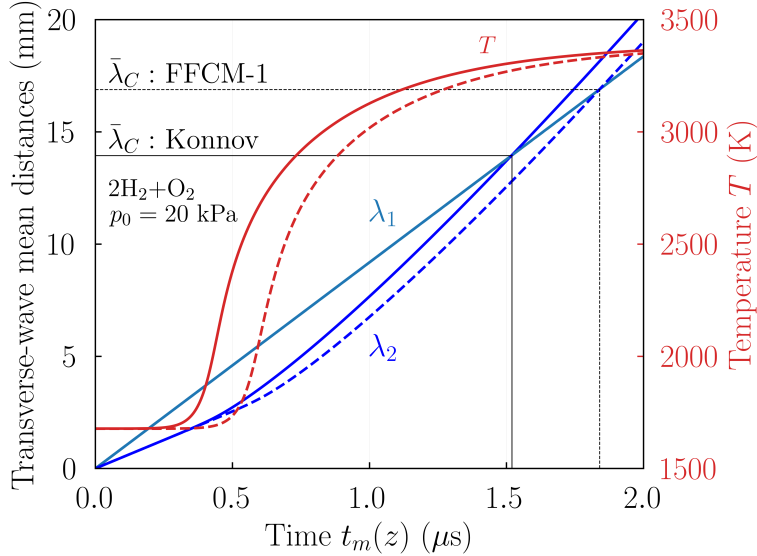


Figure 5: Sensitivities of the material evolutions of the ZND temperature T (red curves, right ordinate), the transverse-waves mean distances λ_1 and λ_2 (Sec. 2, blue and green curves, left ordinate), the cell mean width $\bar{\lambda}_C$ and the ZND complete reaction time t_{ZR} to the chemical kinetic scheme. Full curves: Konnov's scheme, dashed curves: FFCM-1 scheme. The green curves of each scheme are indistinguishable.

Thus, overall, the model predicts the right values and trends of $\bar{\lambda}_C$ for cells independent of the confinement up to reasonably large χ parameters if the chemical kinetic schemes are suitable for the considered mixtures. In these conditions, the relation (7) and the value $\bar{y} = 0.38498$ (20) obtained in the section 3 show that the cellular process should take, on average, $\Delta t_C/t_{ZR} \approx 5.2$ times longer than the ZND process to achieve complete combustion. Why \bar{y} and, therefore, the time ratios $\Delta t_C/t_{ZR}$, $\delta t_{ZR}/t_{ZR}$ and t_{ZI}/t_{ZR} (Sect. 2) are pure numbers, independent of the chemical and physical properties of the mixture, seem to be a mere consequence of the model assumptions, and we have no physical interpretation. In contrast, from the relations (4), (6) and (9) and the basic relation for the burnt volume fraction

$$\bar{v} = \bar{y} \frac{v_{CJ}}{\bar{v}_Z(\bar{y})} \equiv \frac{\delta \ell_{ZR}}{\ell_{ZR}}, \quad \ell_{ZI} = (1 - \bar{v})\ell_{ZR} \quad (22)$$

the length ratios L_C/ℓ_{ZR} , ℓ_{ZI}/ℓ_{ZR} and $\delta \ell_{ZR}/\ell_{ZR}$, where $\ell_{ZI} = U_H t_{ZI}$ and $\delta \ell_{ZR} = U_{CJ} \delta t_{ZR}$ are the thicknesses of the reaction and induction layers ($\ell_{ZR} = \ell_{ZI} + \delta \ell_{ZR}$), depend on the shock and reaction-end properties. Table 2 shows an example. The values of v_H , and v_{CJ} and D_{CJ} are obtained from the ZND calculations, and those of $\bar{\lambda}_C$, ℓ_{ZR} and t_{ZR} are obtained by the procedure described in sections 2 and 3. We emphasize that the model defines thicknesses ℓ_{ZI} and $\delta \ell_{ZR}$ and crossing times t_{ZI} and δt_{ZR} of the induction and main-reaction layers that are larger than those defined from the inflexion points of the profile and evolution of the temperature. Nevertheless, the model gives typical large values of the ratios $\bar{\lambda}_C/\ell_{ZR}$ and $\bar{\lambda}_C/\ell_{ZI}$.

Table 2: Data and calculation results for the mixture $2\text{H}_2 + \text{O}_2$
at $p_0 = 20$ kPa, $T_0 = 293$ K and with the Konnov's scheme [24] (figs. 6)

v_0 (m^3/kg)	v_{H} (m^3/kg)	v_{CJ} (m^3/kg)	D_{CJ} (m/s)	$\bar{\lambda}_{\text{C}}$ (mm)	ℓ_{ZR} (mm)	t_{ZR} (μs)	$\bar{v}_{\text{Z}}(\bar{y})$ (m^3/kg)	\bar{v}	$\bar{\lambda}_{\text{C}}/\ell_{\text{ZR}}$	$\bar{\lambda}_{\text{C}}/\ell_{\text{ZI}}$
10.061	1.827	5.681	2750.9	14.065	1.382	1.528	3.308	0.660	10.177	29.925

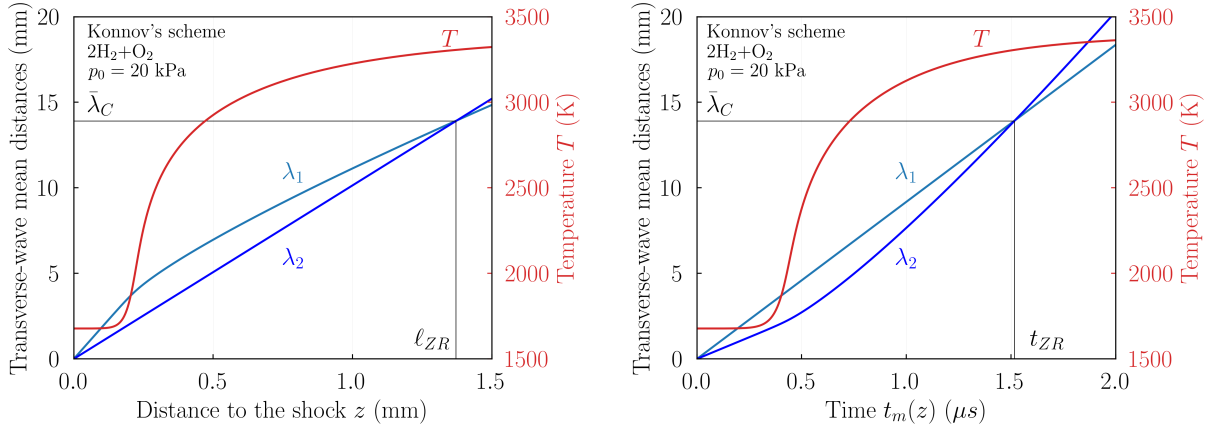


Figure 6: Red curves, right ordinates: ZND profile (left graph) and material evolution (right graph) of the temperature (T). Blue and green curves, left ordinates: transverse-wave mean distances λ_1 and λ_2 as functions of the position (z , blue) and time ($t_m(z)$, green) of a fluid element in the ZND reaction zone relative to the leading shock. The intersections of λ_1 and λ_2 give the cell mean width $\bar{\lambda}_{\text{C}}$ and the ZND complete reaction length ℓ_{ZR} and time t_{ZR} (Sects. 2& 3).

5. Discussion and conclusions

The model predicts well the mean cell width $\bar{\lambda}_C$ up to reasonably large irregularity parameters χ if the chemical kinetic schemes are suitable for the considered mixtures (but cannot –and does not aim to– characterize this front-view irregularity). Therefore, the model confirms the analyses by Short [10] and Radulescu [11, 28], reviewed by Ng and Zhang [2], that larger χ give more irregular lozenges and identify a transition of the combustion process from shock-induced adiabatic ignition for regular-to-irregular lozenges to a more complex one including turbulent diffusion for highly irregular ones.

Adiabatic heating by shock compression is the sole mechanism involved in our approach, which indeed predicts well $\bar{\lambda}_C$ for $\text{H}_2:\text{O}_2$, $\text{H}_2:\text{Air}$, $\text{C}_3\text{H}_8:\text{O}_2$, $\text{C}_3\text{H}_8:\text{Air}$ and $\text{C}_2\text{H}_4:\text{Air}$ mixtures whose lozenges are regular or irregular, and χ small or moderately large. In contrast, the model overestimates $\bar{\lambda}_C$ for $\text{CH}_4:\text{O}_2$ mixtures whose lozenges are highly irregular, and χ very large, *i.e.* 52.5 [2]). In this case, the basic relations for the average reaction rate (7) and the aspect ratio (21) would then no longer hold since they derive from the assumption of a very rapid rate of shock-induced adiabatic combustion in the regions behind the transverse waves and the faster forward waves (Sect. 2).

Therefore, our model provides an indirect means of identifying the mixtures whose detonation reaction zone includes turbulent diffusion since it predicts correct cell mean widths and trends with an adequate chemical kinetic scheme when only adiabatic shock compression is required. In this case, since its implementation is a simple post-processing of ZND profiles, another application is the assessment of the representative capacity of kinetic schemes based on the comparison of calculated mean widths with those obtained from experimental lozenges that are not highly irregular. This contributes to the debates about the representativeness of the experimental cell mean widths $\bar{\lambda}_C$ with a high scatter of measurements and thus about the sufficiency of $\bar{\lambda}_C$ and χ to characterize the geometric properties of these longitudinally highly irregular cells. We emphasize that longitudinal and front-view recordings may not give the same information, for example, respectively, regular lozenges and irregular patterns, depending on the cross-section shape of the tube (Sect. 1).

Theoretical approaches based on perturbation techniques use the ZND steady reaction zone as an initial condition from which small linear perturbations grow, *e.g.*, [15]. Their goal is to select the unstable modes that should evolve into the transverse shocks representing the cellular front in the limits of long times and large transverse dimensions. The expectation is that the number of modes per unit of surface area of the front becomes constant, similarly to multicellular detonations, but too small dimensions limit the number selected, similarly to marginal detonations. Indeed, the experimental cells are independent of the cross-section shapes and areas of sufficiently long and wide detonation tubes [3, 5]. A mathematical estimate of the long-time limit is difficult because the number of modes increases with increasing transverse dimensions. Our approach assumes the opposite basis that the front is multicellular in the sense of both limits and therefore propagates steadily under conditions such that the cellular and the ZND combustion processes are equivalent. Thus our model holds only for multicellular detonations, not for marginal detonations.

One debate is whether selecting 2D modes is a prerequisite for 3D modes. There are three experimental observations. The first is that front views can show patterns regular in a square-section tube and irregular at higher initial pressures in that tube or at the same initial pressure and a larger square-section area. The second observation is that no regular patterns are observed in round tubes and on spherically expanding detonations. Front-view regularity is inherent to marginal detonation regimes in mixtures with light fuels in square or rectangular tubes and not too high initial pressures. That does not represent the physical multicellular (CJ) detonation regime, for which the front views are irregular. The third observation is that, for sufficiently low initial pressures, regular lozenges on longitudinal recordings in square tubes have smaller widths and a thinner aspect ratio $\bar{\lambda}_C/L_C$ than in round tubes of the same cross-section area, and that, for sufficiently high initial pressures, the mean cell widths become independent of the cross-section shape, as shown by the figure 7 in [3]. Therefore, 2D modes, regular or irregular, might not be the right basis for studying 3D modes.

For the situation of irregular front-view patterns independent of the tube cross-section, we have considered the dynamics of the transverse waves to be a stochastic process, both stationary and ergodic. These mathematical definitions are difficult to substantiate formally in the context of detonation dynamics modelling. We can only propose phenomenological elements based on a qualitative understanding of simplified definitions. Stochastic processes involve randomness, and their evolution laws result in probability distributions. They are stationary if the distributions are invariant in time and ergodic if the distributions through space at a given time represent those obtained through time at a given location. The orientations and lengths of the transverse waves, or equivalently the shapes and sizes of the front-view patterns, cannot be the same at a given front position from one experiment to another because of their high sensitivity to the initial conditions. We have assumed this to be correct only within the probabilistic meaning above. Specifically, their successive realizations over the propagation period $\Delta t_C/2$ in the same experiment should form the same distribution as those at the same front position from one experiment to another. We know of none that suggest otherwise at sufficiently long times or large distances from the ignition. No front view shows distributions with patterns that are qualitatively very different in shape and dimension from one experiment to another. In particular, none of the statistical analyses of the numerous cell recordings made so far could have converged on the same $\bar{\lambda}_C$ if this were not the case.

The representation of the cellular front by a hexagonal patterned tessellation should be interpreted as the limiting rearrangement of the cell edges statistically equivalent to their experimental distribution at each instant of time since the Descartes-Euler-Poincaré relation is independent of time. We are looking at the interest of an improved representation by a multi-pattern Voronoi tessellation. We investigate the tentative assumption that the transverse wave dynamics is a Poisson random process both stationary and homogeneous, considering that irregular cells, due to their high sensitivity to initial conditions, have center points randomly distributed, statistically constant in number and which move independently of each other. Table 3 shows the corresponding distribution of the number of edges E of the

patterns obtained explicitly by Calka [29] but recognized implicit in Miles and Maillardet [30]. We observe the predominance of hexagons, then of pentagons and heptagons, about 75%, which supports the representativeness of the hexagon limit used in this work. That also suggests that the mean burnt fraction for this multi-pattern tessellation, calculated from a barycentric rule based on the individual mean burnt fractions and the distribution of the patterns, would be only slightly different from the value 0.385 (20) for the hexagon alone (Sect. 3). We also observe that about 67% of the patterns have at most six edges.

Table 3: Pattern distribution in % as a function of the number of edges E for the homogeneous stationary Poisson process [29, 30]

E	3	4	5	6	7	8	9	10
%	1.1	10.7	25.9	29.5	19.9	9	3	0.7

In conclusion, the model predict correct values and trends of the mean widths $\bar{\lambda}_C$ of detonation cells whose longitudinal soot recordings show longitudinally regular to irregular lozenges independent of the confinement if the chemical kinetic schemes are suitable for the considered mixtures.

Acknowledgements

This work was supported by the Ministry of Higher Education, Research and Innovation, France.

Appendix A. ZND model equations

We summarize below for completeness the basic ZND-model case relevant to this work, namely that for constant-velocity planar detonation in ideal reactive inviscid gases, with detailed chemical kinetic schemes. Higgins [31] and Ng [2] have given comprehensive reviews. The model equations derive from the Euler equations, which express the mass, momentum, and energy balances for the inviscid reactive fluid, simplified by the assumptions that the flow behind the detonation leading shock is one-dimensional planar and steady.

The notation is essentially that introduced in Section 2 and detailed in the nomenclature (B). The origin of the distances x in the laboratory reference frame is an arbitrary initial position $L_0 = 0$ of the shock and the origin of the times t is the instant $t_0 = 0$ when the fluid elements enter the ZND reaction zone. Thus, at an instant $t > 0$, the position of the shock is $L(t) = Dt$ and the distance relative to this position is $z(x, t) = Dt - x$. Steadiness is the invariance of any variable f with respect to $L(t)$ at a constant relative distance z in the reaction zone. With $f(t, x)$ and $f(t, z)$ the corresponding representations, this gives the constraint

$$\left(\frac{\partial f}{\partial t}\right)_x + D \left(\frac{\partial f}{\partial x}\right)_t = \left(\frac{\partial f}{\partial t}\right)_z = 0. \quad (\text{A.1})$$

The Euler equations for one-dimensional planar flow

$$\left(\frac{\partial \rho}{\partial t}\right)_x + \left(\frac{\partial \rho u}{\partial x}\right)_t = 0, \quad (\text{A.2})$$

$$\left(\frac{\partial \rho u}{\partial t}\right)_x + \left(\frac{\partial p + \rho u^2}{\partial x}\right)_t = 0, \quad (\text{A.3})$$

$$\left(\frac{\partial \rho E}{\partial t}\right)_x + \left(\frac{\partial (p + \rho E) u}{\partial x}\right)_t = 0, \quad (\text{A.4})$$

with $E = e + u^2/2$, e the specific internal energy and u the material speed in the laboratory frame, thus reduce to a system of ordinary differential equations

$$\frac{d\mathbf{f}}{dz} = \mathbf{F}(\mathbf{f}, D), \quad \mathbf{f}(z=0) = \mathbf{f}_H(D, p_0, T_0, \mathbf{y}_0), \quad (\text{A.5})$$

where $d./dz \equiv \partial./\partial z)_t$ (since $\partial./\partial t)_z = 0$, (A.1)) denotes the spatial derivatives, \mathbf{f} the vector of the dependent variables, namely p the pressure, ρ the specific mass, $U = D - u$ the material speed in the shock frame, \mathbf{y} the vector of the mass fractions y_k of the K chemical species ($k = 1, K$), $t_m(z)$ the time relative to the shock for a fluid element to reach the position z , and \mathbf{f}_H the values of \mathbf{f} at the shock ($z = 0, t = 0$), which serve as boundary conditions for the integration of the system, given D and the initial pressure p_0 , temperature

T_0 and composition \mathbf{y}_0 . The system writes

$$\frac{dU}{dz} = \frac{\boldsymbol{\sigma} \cdot \mathbf{w}}{1 - M_a^2}, \quad (\text{A.6})$$

$$\frac{dp}{dz} = -\rho U \frac{\boldsymbol{\sigma} \cdot \mathbf{w}}{1 - M_a^2}, \quad (\text{A.7})$$

$$\frac{dv}{dz} = \frac{1}{\rho U} \frac{\boldsymbol{\sigma} \cdot \mathbf{w}}{1 - M_a^2}, \quad (\text{A.8})$$

$$\frac{d\mathbf{y}}{dz} = \frac{\mathbf{w}}{U}, \quad (\text{A.9})$$

$$\frac{dt_m}{dz} = \frac{1}{U}, \quad (\text{A.10})$$

where $v = 1/\rho$ denotes the specific volume, $M_a = U/c$ the flow Mach number, c the frozen sound velocity, $\mathbf{w} = d\mathbf{y}/dt$ the vector of the reaction rates $w_k = dy_k/dt$ (with $d./dt = Ud./dz$ the material derivative), $\boldsymbol{\sigma} \cdot \mathbf{w}$ the thermicity, and $\boldsymbol{\sigma}$ the vector of the thermicity coefficients σ_k . The system is formally closed with hydrodynamic constitutive relations, namely the reaction rates $w_k(p, v, \mathbf{y})$ and the equation of state $e(p, v, \mathbf{y})$ that defines the frozen sound velocity $c(p, v, \mathbf{y})$ and the thermicity coefficients $\sigma_k(p, v, \mathbf{y})$ by

$$c^2 = v^2 \frac{p + \frac{\partial e}{\partial v}}{\frac{\partial e}{\partial p}} \Big|_{p, \mathbf{y}}, \quad \sigma_k = \frac{-v}{c^2} \frac{\partial e}{\partial y_k} \Big|_{p, v, y_{j \neq k}}. \quad (\text{A.11})$$

Calculation codes implement thermal equations of state $h(T, p, \mathbf{n})$ and $v(T, p, \mathbf{n})$, with $h = e + pv$ the specific enthalpy and \mathbf{n} the vector of the mole fractions. Chain rule operations transform their derivatives into the hydrodynamic derivatives in (A.11) [2, 31, 32]. The joint integration of the identity (A.10) with the equations (A.6-A.9) defines the time-position relationships $t_m(z)$ and $z_m(t)$ of a fluid element (Sect.2).

The Euler equations subjected to the steadiness constraint also have first integrals in the form of the Rankine-Hugoniot (RH) relations below, which express the conservation of the mass, momentum and energy surface fluxes from the initial state (subscript 0) through the shock to any distance z or time t relative to the shock in the reaction zone,

$$\rho_0 D = \rho U, \quad (\text{A.12})$$

$$p_0 + \rho_0 D^2 = p + \rho U^2, \quad (\text{A.13})$$

$$h_0 + \frac{1}{2} D^2 = h + \frac{1}{2} U^2. \quad (\text{A.14})$$

The boundary condition on the chemical composition at the shock is often the no-dissociation constraint $\mathbf{y}_H = \mathbf{y}_0$. The RH relations combined with equations of state for h_H and h_0 then determine the boundary value $\mathbf{f}_H(D, p_0, T_0, \mathbf{y}_0)$, and the integration of (A.5) then yields the profiles and evolutions of the corresponding dependent variables. The value of D for the

Chapman-Jouguet detonation is not arbitrary and is a part of the solution. A preliminary estimate is the equilibrium value D_{CJ} obtained by solving the RH relations above supplemented by the chemical equilibrium constraint $\mathbf{A}(T, p, \mathbf{y}) = 0$ on the chemical affinity \mathbf{A} , which defines the composition $\mathbf{y}_{\text{eq}}(T, p)$ at chemical equilibrium, the equilibrium thermal equations of state $h_{\text{eq}}(T, p) = h(T, p, \mathbf{y}_{\text{eq}}(T, p))$ and $v_{\text{eq}}(T, p) = v(T, p, \mathbf{y}_{\text{eq}}(T, p))$, and the equilibrium CJ constraint $U = c_{\text{eq}}(T, p)$, where c_{eq} is the equilibrium sound velocity given by

$$c_{\text{eq}}^2 = v^2 \frac{p + \frac{\partial e_{\text{eq}}}{\partial v}}{\frac{\partial e_{\text{eq}}}{\partial p}} \neq (c^2)_{\text{eq}} = c^2(T, p, \mathbf{y}_{\text{eq}}(T, p)). \quad (\text{A.15})$$

An iterative procedure based on successive integrations of (A.5) initiated with D_{CJ} then aims at framing to a reasonable degree of accuracy which value of D ensures that the derivatives in the ZND system remain physical, that is, bounded, while approaching the sonic locus, since there $1 - M_a = 0$ (or $u + c = D$) and $\mathbf{w} = 0$ (with $\mathbf{A}(T, p, \mathbf{y}) = 0$). That gives the profiles, the evolutions, and the frozen CJ velocity $D_{\text{CJ-f}}$. The latter is different from the equilibrium velocity D_{CJ} because $c_{\text{eq}} \neq (c)_{\text{eq}}$ (A.15), but usually not significantly. Higgins [31] has also discussed the more complex cases of pathological ZND detonations, *e.g.*, $\boldsymbol{\sigma} \cdot \mathbf{w} = 0$ and $\mathbf{w} \neq \mathbf{0}$. We implemented the Caltech ZND code with detailed chemical kinetic schemes and their thermodynamic database taken from the literature (Sect. 4).

Appendix B. Nomenclature

Acronyms and subscripts

0	Initial state and origin of position and time ($L_0 = 0, t_0 = 0$)
($\bar{\quad}$)	Mean value
1D	Mono-dimensional
2D	Two-dimensional
3D	Three-dimensional
B	Burnt gases
C	Cellular process
CJ	Chapman-Jouguet
H	Shocked state
ZND	Zel'dovich - von Neuman - Döring
Z	ZND process
m	Position or time of a fluid element relative to the ZND shock

Physical quantities

\bar{L}_C	Length of the mean cell	m
$\bar{\lambda}_C$	Cell mean width	m
λ	Transverse-wave distance	m
χ	Instability parameter	
a	Cell mean width-to-length aspect ratio ($a = \bar{\lambda}_C/\bar{L}_C$)	
Δt_C	Characteristic time for the length of the mean cell (\bar{L}_C/D_{CJ})	s
D	Detonation velocity	$\text{m} \times \text{s}^{-1}$
A_C	Area of the mean cell	m^2
A_T	Area of the tube	m^2
d_i, d_x	Inner and outer diameters of a hexagon	m

d_{transv}	Transverse dimension of tubes	m
L	Position of the ZND shock in the laboratory frame	m
x	Distances in the laboratory frame	m
z	Distances measured from the ZND shock	m
t	Instant of time	s
p	Pressure	Pa
T	Temperature	K
v	Specific volume	$\text{m}^3 \times \text{kg}^{-1}$
ρ	Specific mass ($\rho = 1/v$)	$\text{kg} \times \text{m}^{-3}$
U	Material speed	$\text{m} \times \text{s}^{-1}$
t_{ZR}	ZND complete reaction time	s
ℓ_{ZR}	ZND complete reaction length ($\ell_{\text{ZR}} = \bar{U}t_{\text{ZR}}$)	m
M	Mass	kg or $\text{kg} \times \text{m}^{-2}$
y	Burnt mass fraction	
\bar{v}	Mean burnt volume fraction	

Mathematical quantities

E	Number of edges	
F	Number of faces	
V	Number of vertices	
μ	Measure of the total hyper-volume	
μ_C	Measure of the non-intersection hyper-volume	
μ_i	Vassallo's non-intersection measure for constant-length segment	
m_i	Non-intersection measure for variable segment length	
r	Non-dimensional segment length	
s	Segment length	m

References

- [1] Y. N. Denisov, Y. K. Troshin, Pulsating and spinning detonation of gaseous mixtures in tubes, *Dokl. Akad. Nauk SSSR* 125 (1959) 110–113.
- [2] H. D. Ng, Detonation instability, in: F. Zhang (Ed.), *Shock Waves Science and Technology Library*, Vol. 6: Detonation Dynamics, Springer Berlin Heidelberg, 2012, pp. 107–212.
- [3] V. Monnier, V. Rodriguez, P. Vidal, R. Zitoun, An analysis of three-dimensional patterns of experimental detonation cells, *Combust. Flame* 245 (2022) 112310.
- [4] J. Crane, J. T. Lipkowicz, X. Shi, I. Wlokas, A. M. Kempf, H. Wang, Three-dimensional detonation structure and its response to confinement, *Proc. Combust. Inst.*, doi:10.1016/j.proci.2022.10.019.
- [5] V. Monnier, V. Rodriguez, P. Vidal, R. Zitoun, Experimental analysis of cellular detonation: a discussion on regularity and three-dimensional patterns, *Proc. 28th Int. Coll. Dynamics Explosions Reactive Systems* (2022), Paper 57.
- [6] R. A. Strehlow, C. D. Engel, Transverse waves in detonations: II. Structure and spacing in $\text{H}_2\text{-O}_2$, $\text{C}_2\text{H}_2\text{-O}_2$, $\text{C}_2\text{H}_4\text{-O}_2$ and $\text{CH}_4\text{-O}_2$ systems, *AIAA J.* 7 (1969) 492–496.
- [7] J. C. Libouton, A. Jacques, P. J. Van Tiggelen, Cinétique, structure et entretien des ondes de détonation, *Act. Coll. Int. Berthelot-Vieille-Mallard-Le Chatelier* (1981) 437–442.
- [8] G. J. Sharpe, J. J. Quirk, Nonlinear cellular dynamics of the idealized detonation model: Regular cells, *Combust. Theor. Model.* 12 (2008) 1–21.
- [9] D. Desbordes, H.-N. Presles, Multi-scaled cellular detonation, in: F. Zhang (Ed.), *Shock Waves Science and Technology Library*, Vol. 6: Detonation Dynamics, Springer Berlin Heidelberg, 2012, pp. 281–338.
- [10] M. Short, G. J. Sharpe, Pulsating instability of detonations with a two-step chain-branching reaction model: theory and numerics, *Combust. Theor. Model.* 7 (2003) 401–416.
- [11] M. I. Radulescu, G. J. Sharpe, D. Bradley, A universal parameter quantifying explosion hazards, detonability and hot spot formation: χ number, in: *Proc. 7th Int. Seminar on Fire and Explosion Hazards*, Research Publishing, 2013, pp. 617–626.
- [12] D. W. Stamps, S. R. Tieszen, The influence of initial pressure and temperature on hydrogen-air-diluent detonations, *Combust. Flame* 83 (1991) 353–364.
- [13] Y. Auffret, D. Desbordes, H.-N. Presles, Detonation structure of $\text{C}_2\text{H}_4\text{-O}_2\text{-Ar}$ mixtures at elevated initial temperature, *Shock Waves* 9 (1999) 107–111.

- [14] Y. Auffret, D. Desbordes, H.-N. Presles, Detonation structure and detonability of $C_2H_2-O_2$ mixtures at elevated initial temperature, *Shock Waves* 11 (2001) 89–96.
- [15] P. Clavin, G. Searby, *Combustion waves and fronts in flows: flames, shocks, detonations, ablation Fronts and explosion of stars*, Cambridge University Press, 2016.
- [16] P. J. Van Tiggelen, J. C. Libouton, Evolution des variables chimiques et physiques à l’intérieur d’une maille de détonation, *Ann. Phys.* 14 (1989) 649–660.
- [17] F. P. Pintgen, J. E. Shepherd, Simultaneous soot foil and plif imaging of propagating detonations, *Proc. 19th Int. Coll. Dynamics Explosions Reactive Systems* (2003), Paper 119.
- [18] F. P. Pintgen, C. A. Eckett, J. M. Austin, J. E. Shepherd, Direct observations of reaction zone structure in propagating detonations, *Combust. Flame* 133 (2003) 211–229.
- [19] J. M. Austin, F. P. Pintgen, J. E. Shepherd, Reaction zones in highly unstable detonations, *Proc. Combust. Inst.* 30 (2005) 1849–1857.
- [20] M. D. Frederick, R. M. Gejji, J. E. Shepherd, C. D. Slabaugh, Time-resolved imaging of the cellular structure of methane and natural gas detonations, *Shock Waves* 32 (2022) 337–351.
- [21] S. F. Vassallo, Buffon’s coin and needle problems for the snub hexagonal tiling, *Adv. Math.: Sci. J.* 10 (2021) 2223–2233.
- [22] R. Takai, K. Yoneda, T. Hikita, Study of detonation wave structure, *Symp. (Int.) Combust.* 15 (1975) 69–78.
- [23] M. Kaneshige, J. Shepherd, Detonation database, California Institute of Technology (2002), Last accessed March 2023.
URL https://shepherd.caltech.edu/detn_db/html/db.html
- [24] F. H. V. Coppens, J. De Ruyck, A. A. Konnov, The effects of composition on burning velocity and nitric oxide formation in laminar premixed flames of $CH_4 + H_2 + O_2 + N_2$, *Combust. Flame* 149 (2007) 409–417.
- [25] Chemical-Kinetic Mechanisms for Combustion Applications, San Diego Mechanism web page, Mechanical and Aerospace Engineering (Combustion Research), University of California at San Diego (2016), Last accessed March 2023.
URL <https://web.eng.ucsd.edu/mae/groups/combustion/mechanism.html>
- [26] G. P. Smith, Y. Tao, H. Wang, Foundational Fuel Chemistry Model Version 1.0 (FFCM-1) (2016), Last accessed March 2023.
URL <https://web.stanford.edu/group/haiwanglab/FFCM1/pages/download.html>

- [27] A. A. Konnov, Yet another kinetic mechanism for hydrogen combustion, *Combust. Flame* 203 (2019) 14–22.
- [28] M. I. Radulescu, G. J. Sharpe, J. H. S. Lee, C. B. Kiyanda, A. J. Higgins, R. K. Hanson, The ignition mechanism in irregular structure gaseous detonations, *Proc. Combust. Inst.* 30 (2005) 1859–1867.
- [29] P. Calka, An explicit expression of the distribution of the number of sides of the typical Poisson-Voronoi cell, *J. Appl. Probab.* 35 (2003) 863–870.
- [30] R. E. Miles, R. J. Maillardet, The basic structures of Voronoi and generalized Voronoi polygons, *J. Appl. Probab.* 19 (1982) 97–111.
- [31] A. Higgins, Steady one-dimensional detonation, in: F. Zhang (Ed.), *Shock Waves Science and Technology Library*, Vol. 6: Detonation Dynamics, Springer Berlin Heidelberg, 2012, pp. 33–100.
- [32] W. Fickett, W. C. Davis, *Detonation*, University of California Press, Ltd., London, 1979.